Acta Crystallographica Section D
**Biological Crystallography**
ISSN 0907-4449

# Observation of time-resolved structural changes by linear interpolation of highly redundant X-ray diffraction data

**Jun Wang and Steven E. Ealick***

Department of Chemistry and Chemical Biology, Cornell University, Ithaca, NY 14853, USA

Correspondence e-mail: see3@cornell.edu

Received 27 May 2004
Accepted 8 July 2004

A new experimental strategy is described for obtaining time-resolved protein structural changes using monochromatic X-ray crystallographic data. The method is based on time-dependent linear interpolation of observed intensity variations during conventional X-ray diffraction data collection. The method benefits from high data redundancy. Although the method was developed to examine time-dependent X-ray-induced crystal decay, it is potentially applicable to a variety of time-dependent crystallographic studies, including structural determination of chemical intermediates in enzyme reactions and X-ray-induced unfolding of proteins with multiple disulfide bonds.

## 1. Introduction

Structural changes at atomic resolution are of great importance in understanding the organization and function of many biological macromolecules. Examples of these structural changes include time-dependent protein modifications during X-ray damage, conformational changes during enzyme catalysis, both global and local changes associated with multi-protein complex formation and protein folding and unfolding. In all these examples, obtaining high-resolution atomic scale molecular structures at various time points has been technically challenging.

Significant efforts are under way within the crystallography community to observe time-dependent structural changes during photochemical reactions (Cianci *et al.*, 2002; Rajagopal & Moffat, 2003; Schotte *et al.*, 2003). The lifetimes of these photoactivated structures are usually of the order of hundreds of picoseconds and thus require a pump-probe data-measurement technique. In photosensitive proteins, time-resolved white-beam Laue techniques have been used to elucidate the structural basis of a biochemical mechanism after pulsed laser excitation. Time-resolved diffraction experiments have also been carried out using optical light as a pump and polychromatic synchrotron X-ray pulses as a probe to study structural changes in the myoglobin–CO complex (Srajer *et al.*, 1996).

In some enzymatic reactions, the reaction rate can be slowed under certain conditions or enzyme intermediates can be trapped so that conventional crystallography can be used to obtain the structures that are essential for understanding enzyme mechanisms. However, during crystallographic data collection X-ray-generated photoelectrons may interfere with enzyme reactions, thus making observation of the intermediates difficult. One solution to this problem is a multi-crystal data-collection strategy that was developed to isolate

X-ray-driven catalytic effects during data collection, leading to the determination of the intermediate structures (Berglund *et al.*, 2002). In some cases, the photoelectrons generated by X-rays can directly trigger the enzyme reaction and production of intermediates (Schlichting *et al.*, 2000). For this purpose, radiation burns at a long X-ray wavelength are usually introduced between two measured data sets. The structural changes induced by radiation damage can also be used to determine phase angles (Banumathi *et al.*, 2004).

Both the multiple-crystal method and the radiation-burn method are special techniques designed to cause specific changes in a protein structure and in both cases certain complications may exist in an experiment, even though the methods are cleverly designed. For example, long exposure with long-wavelength X-rays may cause undesired structure changes that may complicate the interpretation of the intermediate structure. The use of multiple crystals may introduce variations in crystal quality, size and shape that may lead to unwanted systematic effects in the data set.

In this article, we present a new straightforward data-reduction method to take into account structural changes arising from chemical reaction or X-ray-induced effects within a single data set. We used X-ray-induced structural changes in a single crystal of insulin to demonstrate our method. We show significant intensity changes for many unique reflections arising from radiation exposure during a single data-collection run. In our new experimental strategy, these intensity changes can be taken into account using a linear model that leads not only to a zero-dose structure as discussed by Diederichs *et al.* (2003) but also to a series of time-resolved high-resolution crystal structures that are otherwise not available using conventional crystallography.

## 2. Experiment

For these experiments, we chose to study the cubic form of porcine pancreatic insulin ($C_{256}H_{381}N_{65}O_{76}S_6$; 5778 Da) purchased from Sigma. Insulin has three disulfide bonds that are sensitive to X-ray damage. Crystals were prepared using the hanging-drop method based on a modification of the previously published dialysis conditions (Dodson *et al.*, 1978). The well solution consisted of 0.2 *M* $Na_2HPO_4$, 0.01 *M* EDTA, 0.1 *M* bicine, 0.5%(*w*/*v*) xylene pH 9.4 and the protein concentration was 15–20 mg ml$^{-1}$. Hanging drops were prepared by mixing 1 µl protein solution and 1 µl well solution. Crystals appeared after 20 h at room temperature and belong to cubic space group $I2_13$, with unit-cell parameter $a$ = 78.1 Å.

Diffraction data were collected at the Northeastern Collaborative Access Team (NE-CAT) beamline 8-BM at the Advanced Photon Source, Argonne National Laboratory. A crystal of dimensions 0.2 × 0.3 × 0.3 mm was rapidly frozen after first soaking in a solution consisting of the well solution plus 30% glycerol (Dr Zhijie Liu, personal communication) and then mounted in a nitrogen-gas stream at a temperature of 100 K using an Oxford Cryosystems device. A single data set was measured at a wavelength of 1.5 Å and a sample-to-detector distance of 20 cm. The detector was offset vertically for the purpose of collecting data to 1.56 Å resolution. The total rotation range was 360°, 1° per frame, with an exposure

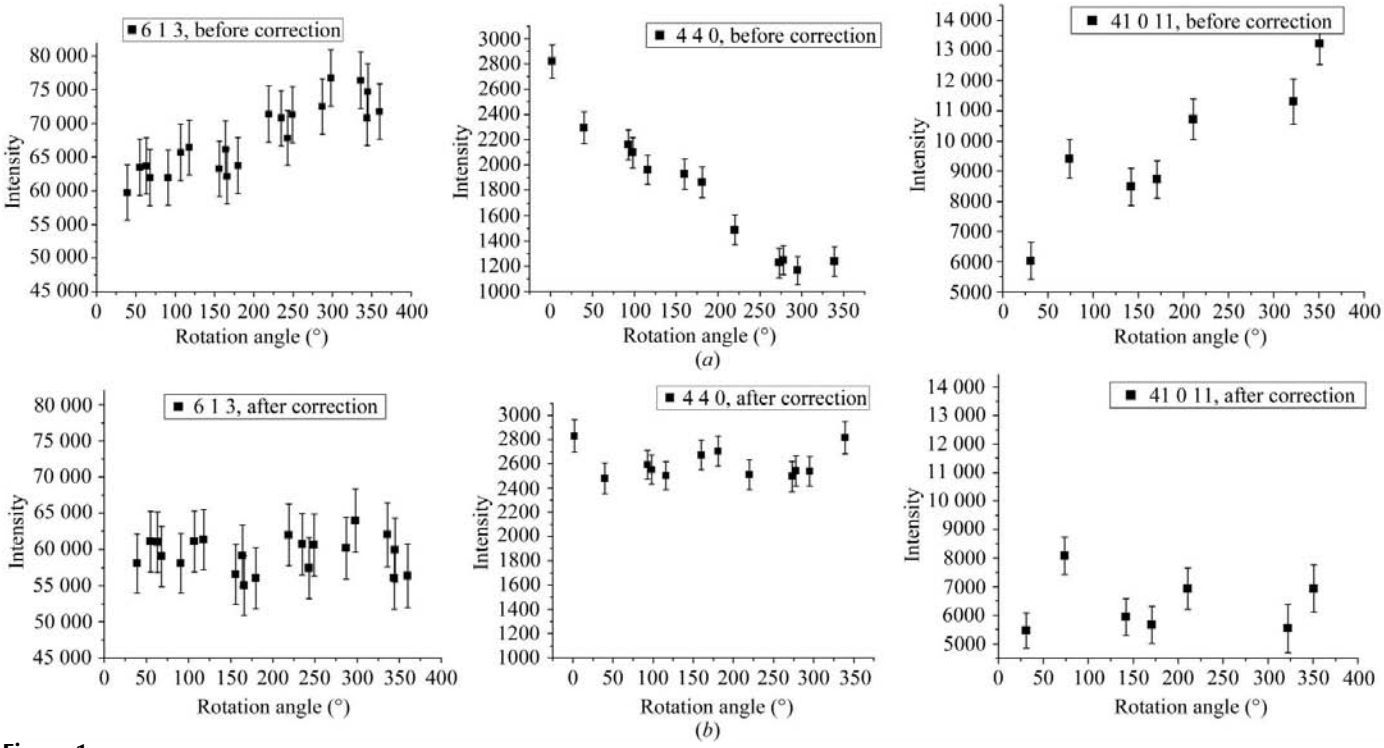


**Figure 1**
Examples of intensity variations of equivalent observations in the insulin data. (*a*) Three reflections before corrections for radiation decay. (*b*) The same reflections after intensity corrections to $t$ = 0. These reflections show extreme examples of the changes caused by radiation-induced bond breaking.

**Table 1**
Data-processing statistics as a function of resolution.

| Resolution shell | $I/\sigma(I)$ | $R$ factor (%) | Completeness (%) | Redundancy |
|---|---|---|---|---|
| 50–3.36 | 39.5 | 4.2 | 86.3 | 18.1 |
| 3.36–2.67 | 47.1 | 4.5 | 99.6 | 20.3 |
| 2.67–2.33 | 52.5 | 5.0 | 100.0 | 20.5 |
| 2.33–2.12 | 50.9 | 6.0 | 100.0 | 18.4 |
| 2.12–1.97 | 46.5 | 6.5 | 100.0 | 17.6 |
| 1.97–1.85 | 40.3 | 6.8 | 100.0 | 15.0 |
| 1.85–1.76 | 34.4 | 6.6 | 100.0 | 13.7 |
| 1.76–1.68 | 27.9 | 6.6 | 100.0 | 12.6 |
| 1.68–1.62 | 20.6 | 7.8 | 98.3 | 11.6 |
| 1.62–1.56 | 14.1 | 10.2 | 98.4 | 10.5 |

time of 20 s. Data were recorded using an ADSC Quantum 315 detector and because the detector was vertically offset only half of the diffraction pattern was recorded.

8-BM is a bending-magnet beamline. The flux is about $10^{11}$ photons $s^{-1}$ with an $0.3 \times 0.3$ mm beam size at the crystal position. The linear absorption coefficient for cubic insulin is $10.47\ cm^{-1}$ as calculated using the website http://www.cxro.lbl.gov with an estimation of protein crystal density of $1.3\ g\ cm^{-3}$. Based on a dose definition as energy absorbed per unit mass, the total dose of the crystal absorbed is $10^7$ Gy for the entire 360° data set.

## 3. Method

X-ray intensity data for cubic insulin were integrated and globally scaled using *HKL*2000 (Otwinowski & Minor, 1997). The scaling was performed without merging symmetry-equivalent observations in order to investigate the intensity variations of a unique reflection as a function of increasing accumulated exposure time. After global scaling, it can be seen that some unique reflections exhibit decreasing intensities with increasing accumulated exposure time, while others show increasing intensities, indicating internal structural changes resulting from X-ray exposure. Some extreme examples of such intensity changes are shown in Fig. 1(*a*).

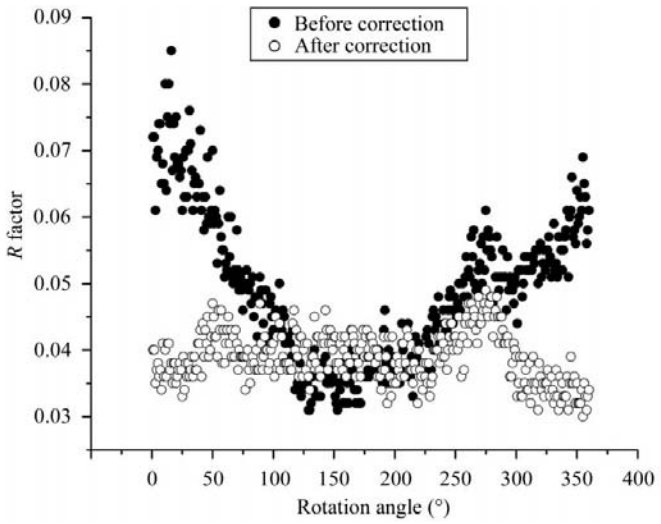


**Figure 2**
$R$ factor as a function of rotation angle. The filled circles are before correction and the open circles are after correction to $t = 0$.

**Table 2**
Distribution of the initial *HKL*2000 scale factor as a function of rotation angle and resolution.

| Resolution (Å) | Rotation range† 1 | 2 | 3 | 4 | 5 | 6 | 7 | 8 | 9 | 10 |
|---|---|---|---|---|---|---|---|---|---|---|
| 50–3.36 | 1.079 | 0.987 | 0.932 | 0.996 | 1.044 | 1.015 | 0.973 | 0.942 | 1.020 | 1.031 |
| 3.36–2.67 | 1.154 | 1.024 | 0.947 | 1.013 | 1.058 | 1.009 | 0.935 | 0.930 | 1.002 | 0.992 |
| 2.67–2.33 | 1.190 | 1.009 | 0.966 | 1.014 | 1.091 | 1.018 | 0.946 | 0.917 | 0.975 | 1.009 |
| 2.33–2.12 | 1.265 | 1.034 | 0.819 | 1.048 | 1.190 | 1.000 | 0.903 | 1.077 | 1.006 | 1.031 |
| 2.12–1.97 | 1.363 | 1.115 | 0.789 | 0.929 | 1.067 | 1.010 | 0.964 | 1.026 | 1.202 | 1.308 |
| 1.97–1.85 | 1.648 | 1.362 | 0.972 | 1.069 | 1.093 | 1.074 | 0.970 | 0.967 | 1.255 | 1.007 |
| 1.85–1.76 | 1.182 | 1.003 | 0.956 | 0.891 | 1.078 | 1.486 | 1.345 | 0.940 | 1.491 | 1.902 |
| 1.76–1.68 | 1.586 | 1.724 | 1.170 | 0.898 | 1.316 | 1.787 | 1.372 | 0.945 | 1.129 | 1.497 |
| 1.68–1.62 | 2.847 | 1.478 | 1.958 | 1.253 | 0.936 | 2.936 | 1.919 | 0.700 | 1.536 | 4.348 |
| 1.62–1.56 | 7.258 | 3.137 | 1.819 | 1.893 | 4.167 | 2.511 | 3.921 | 1.796 | 6.134 | 2.366 |

† Each rotation range represents 36° and 720 s of X-ray exposure [$\varphi_{start} = (n-1) \times 36°$; $\varphi_{end} = n \times 36°$].

Data-processing statistics are shown in Table 1. Although 360° of data were collected, which should lead to a redundancy of 48, the average redundancy is only 16 because the detector was offset vertically and less than half the solid angle of diffraction was recorded. The total number of unique reflections is 11 266. Table 2 shows the *HKL*2000 scale factor as a function of time (rotation angle) and resolution. The global intensity decay is about 19, 23 and 25% for low-, medium- and high-resolution data, respectively. Fig. 2 shows the $R$ factor as a function of time (rotation angle) before and after correction for radiation decay. The U-shaped $R$-factor curve ($\chi^2$ shows a similar U-shape) before correction indicates the presence of time-dependent radiation damage.

### 3.1. Linear fits of unique reflection data

Based on the observations shown in Fig. 1(*a*), we developed the program *FitScale* to fit all of the observations of each unique intensity as a function of time. A linear least-squares model based on the idea of Diederichs *et al.* (2003) was used; however, we generalized the expression to obtain the interpolated values of each observation at any time $t$ rather than at zero dose.

Assuming $n$ observations for each unique reflection $j$, the least-squares function for fitting a straight line to observed intensities, $I_{ij}$, is given by

$$\chi_j^2 = \sum_i \left[ \frac{1}{\sigma_{ij}^2} (I_{ij} - c_j - k_j t_{ij})^2 \right], i = 1, 2, \ldots, n, \qquad (1)$$

where $t_{ij}$ is the time at which intensity $I_{ij}$ is measured and $\sigma_{ij}$ is the standard deviation of the intensity.

The slope $k$, which we call the time-dependent factor, and its uncertainty can be calculated according to standard procedures (Bevington, 1969). The value of $c_j$ represents the intensity at zero dose.

### 3.2. Time-resolved structure

The intensities $I_{ij}$ at a given accumulated exposure time $t$ are given by (2) and the standard deviations $\sigma_{ij}$ by (3),

$$I_{ij}^{\rm corr}(t) = I_{ij} + k_j \Delta t, \quad (2)$$

$$\sigma_{ij}^{\rm corr} = (\sigma_{ij}^2 + \sigma_{k_j}^2 \Delta t^2)^{1/2}, \quad (3)$$

$$\Delta t = t - t_{ij}. \quad (4)$$

Here, we have assumed that the intensities within each Friedel pair have the same time-dependent factor $k_j$. If the anomalous signal is relatively strong, then it may be possible to deduce separate slopes for the $(hkl)$ and $(\overline{hkl})$ reflections. For further scaling, each individual observation is interpolated to time $t$. This procedure separates the treatment of systematic errors, such as variation in the incident beam intensity or crystal miscentering, and the time-dependent structural changes that are obtained by comparing data sets corrected to different times.

The intensities calculated from (2) are then scaled using *SCALA* (Collaborative Computational Project, Number 4, 1994). The final merged data are then used for structure determination and refinement. Using the corrections derived by interpolation to time $t$, the structural changes induced by X-ray exposure in this insulin example can be investigated at different times. In the more general application, it provides a way to obtain structural snapshots at different time points for any structural change (*e.g.* changes during a chemical reaction that occur during the time course of the X-ray diffraction experiment).

## 4. Results

### 4.1. Statistical distribution of individual scaling

Fig. 1(*b*) shows the changes of intensities of individual measurements *versus* time $t$ after applying the corrections. The $k$ factors for these reflections are extreme and a statistical analysis of the $k$ factors for the complete data set are given in Tables 3 and 4. For this purpose, we use the intensity-normalized slope $K_j$ ($K_j = k_j/c_j$, where $c_j$ is the zero dose intensity). The average $K$ values, the standard variation and the range ($K_{\rm max} - K_{\rm min}$) are listed in Table 3 as a function of resolution. The histogram distribution of $K$ is shown in Table 4. The improvement in the intensity values is illustrated by $R$ factors (open circle in Fig. 2) from *SCALA* after the intensity correction.

In this procedure, we only determine the effect of X-ray irradiation on structural changes, so we separate the time-dependent structural changes from any other possible time-dependent instrument changes that would be considered as systematic error. The often large deviations among equivalent observations owing to radiation-induced structural changes are corrected, while fluctuations generated by experimental systematic errors are taken into account by the scaling program, in our case, *SCALA*.

**Table 3**
Statistics of intensity-normalized $K$ factor as a function of resolution.

| Resolution (Å) | $\langle K \rangle$ † ($\times 10^{-5}$) | r.m.s.$\Delta K$ ‡ ($\times 10^{-3}$) | $K$ range § ($\times 10^{-3}$) |
|---|---|---|---|
| 50–3.36 | 38.9 | 3.4 | 81 |
| 3.36–2.67 | 15.7 | 2.4 | 75 |
| 2.67–2.33 | 20.1 | 1.8 | 41 |
| 2.33–2.12 | 25.4 | 2.2 | 47 |
| 2.12–1.97 | 18.7 | 1.7 | 36 |
| 1.97–1.85 | 75.5 | 1.2 | 16 |
| 1.85–1.76 | 27.0 | 2.7 | 52 |
| 1.76–1.68 | 10.9 | 1.6 | 34 |
| 1.68–1.62 | 40.2 | 3.3 | 110 |
| 1.62–1.56 | 76.1 | 5.9 | 111 |

† $\langle K \rangle = \sum K_i/n$. ‡ r.m.s.$\Delta K = [\sum (K_i - \langle K \rangle)^2/n]^{1/2}$. § $K$ range $= K_{\rm max} - K_{\rm min}$.

**Table 4**
Distribution of the intensity-normalized $K$ factor ($\times 10^{-3}$) as a function of resolution shells.

| | $K$ range | | | | | | | | | |
|---|---|---|---|---|---|---|---|---|---|---|
| Resolution (Å) | −4.5 | −3.5 | −2.5 | −1.5 | −0.5 | 0.5 | 1.5 | 2.5 | 3.5 | 4.5 |
| 50–3.36 | 0 | 1 | 8 | 48 | 453 | 502 | 70 | 20 | 9 | 2 |
| 3.36–2.67 | 0 | 1 | 9 | 54 | 527 | 443 | 55 | 18 | 5 | 3 |
| 2.67–2.33 | 0 | 0 | 15 | 37 | 514 | 445 | 60 | 30 | 5 | 4 |
| 2.33–2.12 | 0 | 3 | 14 | 58 | 487 | 425 | 83 | 24 | 14 | 2 |
| 2.12–1.97 | 0 | 2 | 18 | 79 | 457 | 438 | 74 | 23 | 9 | 7 |
| 1.97–1.85 | 1 | 4 | 11 | 86 | 507 | 388 | 71 | 27 | 7 | 9 |
| 1.85–1.76 | 2 | 7 | 13 | 95 | 470 | 387 | 78 | 26 | 18 | 5 |
| 1.76–1.68 | 4 | 7 | 18 | 107 | 434 | 385 | 88 | 32 | 16 | 9 |
| 1.68–1.62 | 3 | 10 | 22 | 77 | 371 | 409 | 112 | 39 | 20 | 10 |
| 1.62–1.56 | 5 | 13 | 20 | 105 | 324 | 370 | 118 | 42 | 24 | 11 |

**Table 5**
Success rate of *SnB* solution of S atoms location for the structures at different accumulated exposure times.

| $t$ (s) | Success rate (%) |
|---|---|
| 0 | 2 |
| 1800 | 1.4 |
| 3600 | 1.2 |
| 5400 | 1 |
| 7200 | 0.6 |

### 4.2. Locating S atoms as a function of time

Several corrected data sets at different accumulated exposure times $t$ were deduced using (2) and the single insulin data set. To investigate the effects of disulfide-bond breaking on sulfur anomalous scattering, we determined the structure of cubic insulin at different exposure times. *SnB* (Weeks & Miller, 1999) was used to locate the six S atoms for each data set. The *SnB* results at $t = 0$, 1800, 3600 and 7200 s are shown in Table 5. Although the six S atoms were located for all deduced data sets from $t$ = 0–7200 s, the success rate decreased with increasing radiation dosage. This is an indication of the gradual disordering of the S atoms during data collection. Using the positions of the six S atoms, single-wavelength anomalous diffraction (SAD) phasing was performed using *CNS* (Brünger *et al.*, 1998) and the experimental phases were improved by density modification with solvent flipping (Abrahams & Leslie, 1996), assuming 61% solvent in the crystal. The experimental density map for $t = 0$ is shown in

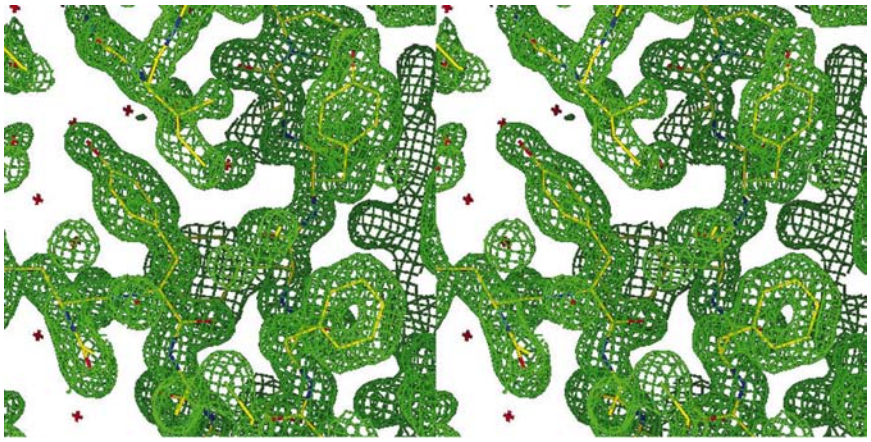

**Figure 3**
Stereoview of experimental density map of insulin at $t = 0$.

Fig. 3. The experimental phases for accumulated exposure time $t$ at 0, 1800, 3600 and 7200 s were determined similarly and the best map was obtained at $t = 0$.

### 4.3. Time-resolved difference Fourier maps

In order to investigate the specific structural changes induced by X-ray exposure as a function of accumulated exposure time $t$, difference Fourier maps are calculated to show the changes using the *CCP*4 *FFT* program (Collaborative Computational Project, Number 4, 1994). In order to avoid model bias, $F_{obs}(t) - F_{obs}(0)$ was used to visualize the differences (Stryer *et al.*, 1964) using phase information from the structure at $t = 0$. Fig. 4 shows the negative (pink) and positive (cyan) electron-density maps ($\pm 6\sigma$) near the three disulfide bonds at time $t = 0$, 1800, 3600, 5400 and 7200 s, respectively. Fig. 4 shows that the negative-density peaks increase with accumulated exposure time resulting from a gradual loss of order in the disulfide bonds owing to radiation exposure. The positive peaks are less evident because the S atoms of the broken disulfide bridge are probably distributed over multiple positions and have high $B$ factors.

It is also possible to determine the order of disulfide-bond breaking in the crystal structure. As illustrated in Fig. 4, the CysA20—CysB19 disulfide bond is the first to show evidence of conformational change, followed by CysB7—CysA7 and with CysA6—CysA11 last. Since folding of disulfide-rich proteins depends on the order of formation of the disulfide bonds, Fig. 4 indicates that disulfide bonds unfolding in the crystal, induced by radiation exposure, may provide information about the order of formation of these bonds during protein folding.

It is also interesting to note differences in the behavior of the three disulfide bonds in cubic insulin. The two disulfide bonds at CysA7—CysB7 and CysA20—CysB19 exhibit similar features arising from irradiation. The S atoms show negative peaks at their original positions, but no positive peaks appear. This may arise from the fact that these two disulfide bonds are both exposed to solvent and thus the S atoms can easily become disordered after the bond is broken. In contrast, CysA6—CysA11, which is buried, shows accumulation of positive density near CysA6. This suggests that a shift of the S atom to a new ordered position occurs after the disulfide bond is broken. This could be a consequence of tighter packing that occurs in the interior of the protein structure.

It is also worth noting that the changes between $t = 5400$ and 7200 s appear to be smaller than for previous panels. This suggests that X-ray-induced opening of disulfide bonds is complex and may lead to metastable intermediate structures before the crystal becomes further damaged and disordered owing to irradiation. A complete understanding of this effect will require further theoretical and experimental studies. We plan to investigate this effect by observing the trend of intensity changes with a much longer data-collection time that would cover both the initial structural changes and the eventual crystal decay owing to irradiation within a single data set.

In addition to peaks near the S atoms, which were the largest features in the difference maps, a number of smaller peaks appeared. The largest of these were peaks of $-5.5\sigma$ each near the carboxylate group of GluB13 and the carbonyl O atom of LeuB6. The next seven largest features ($>4\sigma$ or $<-4\sigma$) were associated with the carbonyl O atoms of AsnA21, ValB12, AlaB14, GlnB4, LeuA13 and the amide N atoms of TyrA14 and LeuB15. All nine peaks increased in magnitude with time. It is possible that these peaks are secondary effects associated with backbone movements that occur after disulfide-bond breaking or, in the case of GluB13, side-chain decarboxylation.

## 5. Discussion

We have presented an analytical method to extract time-dependent structural changes from a conventional monochromatic data set using a single crystal. A key feature of the method is the interpolation of each measurement to time $t$ prior to final scaling. This approach allows the separation of time-dependent structural changes and time-dependent systematic errors such as variation in the incident beam intensity. In the case of cubic insulin, the data redundancy is high (average of 16) and provides a favorable case. However, we believe that the method may be more universally applicable to all crystal space groups and redundancy can be improved by measuring more than 360° of data. Data redundancy is one of the considerations in choosing the simple linear model presented here and is also consistent with the trends of individual reflections shown in Fig. 1(*a*). However, our method does not exclude the use of other data models if a sufficient number of equivalent observations for each unique reflection are available. Furthermore, it may be possible to

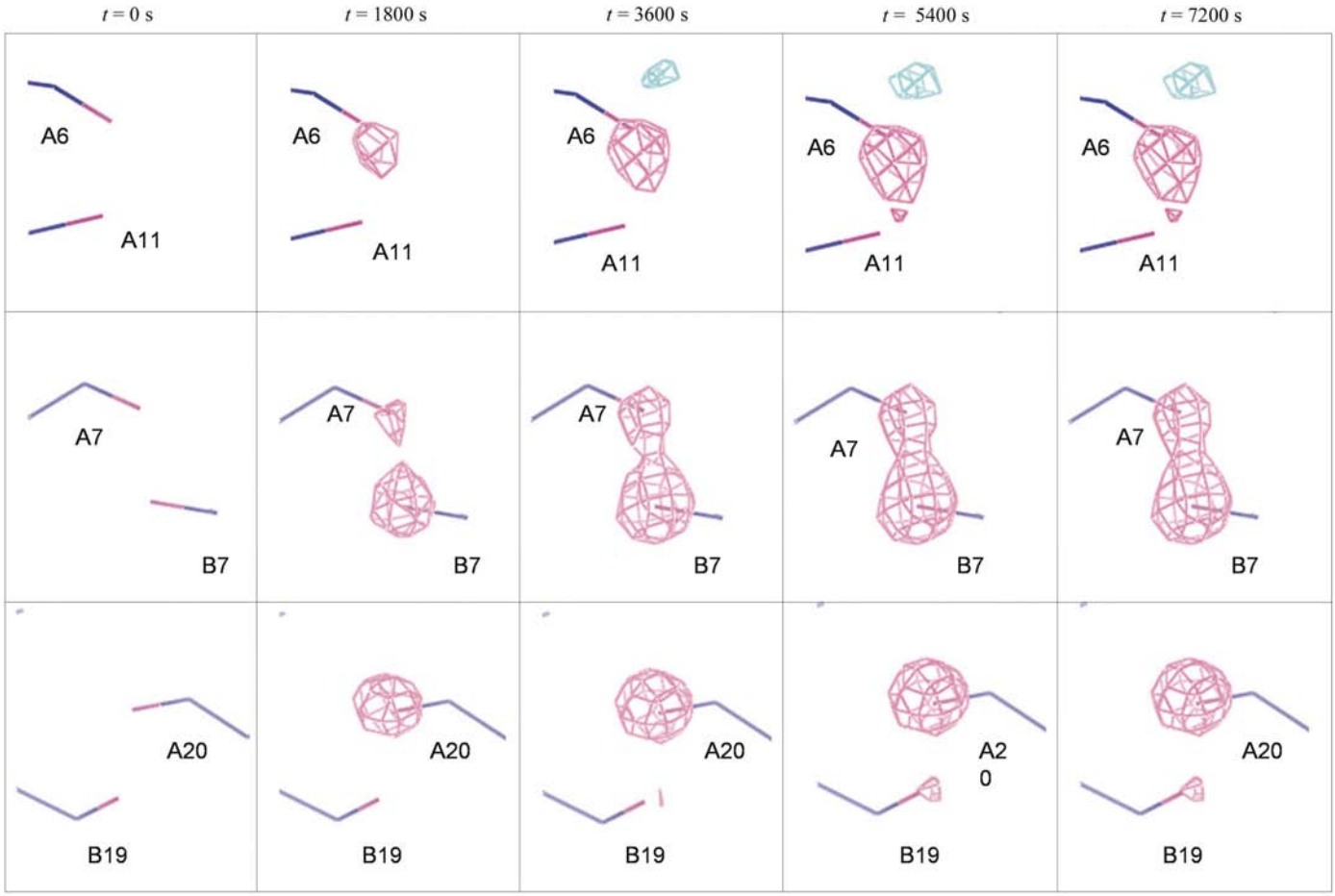


**Figure 4**
Time-resolved difference Fourier maps $[F_{obs}(t) - F_{obs}(0)]$ at $t$ = 0, 1800, 3600, 5400 and 7200 s. Pink represents negative density ($-6\sigma$) and cyan represents positive density ($+6\sigma$). The top row shows the CysA6—CysA11 disulfide bond, the middle row shows changes in the CysA7—CysB7 disulfide bond and the bottom row shows the CysB19—CysA20 disulfide bond.

use the global data set to determine local trends for time-dependent factors of individual reflections.

The method described here is not limited to X-ray-induced structural changes. In principle, any structural changes occurring during data collection can be characterized with the approach described here. Enzyme reactions in the crystalline phase can often be slowed by lowering the temperature, changing the pH, mutating active-site residues or using slow substrates. In addition, undulator beamlines at third-generation synchrotron sources offer the possibility of greatly accelerating data-collection rates. Nonetheless, several issues must be resolved in order to apply our method to time-resolved structure analysis of enzymes. These issues include synchronizing active sites within a protein crystal and minimizing structural ensembles as the reaction proceeds. In the future, the time-resolved experimental strategy described here will require auxiliary techniques such as single-crystal microspectrophotometry to correlate measured structural transitions with measured electronic transitions. An additional complication will be separating time-dependent structural changes caused by chemical reactions and the time-dependent structural changes caused by X-ray damage.

## 6. Conclusion

We have presented a new strategy using standard monochromatic X-ray crystallographic experiments to allow direct observations of structural changes on an atomic scale in a protein crystal. Although the X-ray-induced structure described here is the result of radiation damage, the strategy provided in this article is generally applicable to time-dependent structural changes such as those that occur during enzyme catalysis. The sequence of disulfide-bond breaking may also have implications for protein-folding pathways. Further experiments using other systems are under way.

The authors would like to thank Dr Qun Shen and Dr Craig Ogata for helpful discussions and comments. This work is supported by NIH grant RR-15301 from the National Center for Research Resources of the National Institutes of Health.

## References

Abrahams, J. P. & Leslie, A. G. W. (1996). *Acta Cryst.* D**52**, 30–42.
Banumathi, S., Zwart, P. H., Ramagopal, U. A., Dauter, M. & Dauter, Z. (2004). *Acta Cryst.* D**60**, 1085–1093.

Berglund, G. I., Carlsson, G. H., Smith, A. T., Szoke, H., Henriksen, A. & Hajdu, J. (2002). *Nature (London)*, **417**, 463–468.
Bevington, P. R. (1969). *Data Reduction and Error Analysis for the Physical Sciences.* New York: McGraw–Hill.
Brünger, A. T., Adams, P. D., Clore, G. M., DeLano, W. L., Gros, P., Grosse-Kunstleve, R. W., Jiang, J.-S., Kuszewski, J., Nilges, M., Pannu, N. S., Read, R. J., Rice, L. M., Simonson, T. & Warren, G. L. (1998). *Acta Cryst.* D**54**, 905–921.
Cianci, M., Rizkallah, P. J., Olczak, A., Raftery, J., Chayen, N. E., Zagalsky, P. F. & Helliwell, J. R. (2002). *Proc. Natl Acad. Sci. USA*, **99**, 9795–9800.
Collaborative Computational Project, Number 4 (1994). *Acta Cryst.* D**50**, 760–763.
Diederichs, K., McSweeney, S. & Ravelli, R. B. G. (2003). *Acta Cryst.* D**59**, 903–909.
Dodson, E. J., Dodson, G. G., Lewitova, A. & Sabesan, M. (1978). *J. Mol. Biol.* **125**, 387–396.
Otwinowski, Z. & Minor, W. (1997). *Methods Enzymol.* **276**, 307–326.
Rajagopal, S. & Moffat, K. (2003). *Proc. Natl Acad. Sci. USA*, **100**, 1649–1654.
Schlichting, I., Berendzen, J., Chu, K., Stock, A. M., Maves, S. A., Benson, D. E., Sweet, R. M., Ringe, D., Petsko, G. A. & Sligar, S. G. (2000). *Science*, **287**, 1615–1622.
Schotte, F., Lim, M., Jackson, T. A., Smirnov, A. V., Soman, J., Olson, J. S., Phillips, G. N. Jr, Wulff, M. & Anfinrud, P. A. (2003). *Science*, **300**, 1944–1947.
Srajer, V., Teng, T.-Y., Ursby, T., Pradervand, C., Ren, Z., Adachi, S., Schildkamp, W., Bourgeois, D., Wulff, M. & Moffat, K. (1996). *Science*, **274**, 1726–1729.
Stryer, L., Kendrew, J. C. & Watson, H. C. (1964). *J. Mol. Biol.* **8**, 96–104.
Weeks, C. M. & Miller, R. (1999). *J. Appl. Cryst.* **32**, 120–124.